UNCERTAINTY IN IMAGE-TO-PHYSICAL REGISTRATION FOR SOFT-TISSUE IMAGE GUIDED SURGERY

By

Jarrod Collins

Thesis
Submitted to the Faculty of the
Graduate School of Vanderbilt University
in partial fulfillment of the requirements
for the degree of

MASTER OF SCIENCE
in

Biomedical Engineering
December, 2015
Nashville, Tennessee

Approved: Date:

_____ _____
Robert L. Galloway Jr. PhD

_____ _____
Michael I. Miga PhD

ACKNOWLEDGEMENTS

I would like to thank my advisor Dr. Michael Miga for his guidance and insight. I would also like to thank Dr. Jared Weis and Dr. Logan Clements for their advice and discussions which helped to define the methods of this research. I am thankful to Dr. Bob Galloway for this critiques in writing this document and Dr. Benoit Dawant for the techniques that he instructed throughout his advanced image processing course. I am especially grateful to the members of Biomedical Modeling Laboratory at Vanderbilt for their support, friendship, and comic relief. I am also thankful for Dr. Bill Jarnagin and Dr. Amber Simpson for their collection of our clinical data. Most of all I am thankful for my closest friend, Toral Patel, for her patience and encouragement through this process.

TABLE OF CONTENTS

Page

LIST OF TABLES

Table Page

LIST OF FIGURES

Figure Page

CHAPTER 1

Introduction

1.1 Motivation

It is estimated that over 50% of a projected 135,260 cases of colorectal cancer in the United States for the next year will develop hepatic metastases.[1] Twenty percent of those cases will develop metastases solely in the liver.[2-3] The median survival window for untreated disease is 6-12 months and patients rarely survive beyond 3 years.[4-5] Furthermore, with a highly variable 5-year survival rate of 25-58%[6-11], an additional 35,660 cases of primary liver cancer are projected.[12] Multiple treatment options exist, including resection, ablation, and chemotherapy. Surgical resection is the preferred mode of treatment and has been particularly effective in conjunction with other methods. However only 15-30% of patients are eligible for resection based on factors such as tumor size, frequency, or proximity to delicate or vital structures.[13-14] Ablative techniques have provided a promising alternative, however both ablation and resection are highly reliant on accuracy and physician expertise.[15-17] The ability of a physician to localize treatment with a high degree of accuracy could potentially lead to a higher rate of negative margins, a better ability to treat difficult disease presentations, and improved patient outcome. Image-guided surgical methods have been proposed, and investigated, as techniques to increase the localization accuracy, and therefore utility, of hepatic cancer treatments such as resection and ablation.

Registration serves as the fundamental method to image-guided surgical techniques and is a mathematical technique which is used to map the intraoperative organ state to preoperative organ images. This mapping allows for real-time display of the position of surgical tools or intraoperative imaging, such as ultrasound, in reference to the preoperative diagnostic image data. The determination of an accurate image-to-physical-space registration provides crucial navigational

information in targeting subsurface locations or avoiding vital healthy anatomy. A proper registration serves to increase the amount and fidelity of information available to the physician.

Surface-based registration techniques are currently used to determine an image-to-physical-space mapping. One example that is commercially used within the context of image-guided liver surgery is the salient-feature weighted iterative closest point (ICP) algorithm presented by Clements et al.[18] In this example, intraoperative data is collected by a passive optically tracked stylus. Alternative strategies using an optically tracked laser range scanner and conoscopic holography range finders have also been utilized to acquire 3D surface digitizations.[19-20] Additionally, multiple groups have investigated the use of tracked ultrasound for sparse surface data acquisition.[21-22] While interesting, we will limit our discussion to Clements et al. approach as it is part of an FDA approved soft-tissue guidance system. In this approach, the current clinical protocol for image-to-physical registration in hepatic cases begins with the image-space designation of anatomical regions such as the falciform ligament and inferior ridges. Intraoperatively, the corresponding physical-space location of the features are digitized. The salient-feature ICP method provides a robust rigid alignment which utilizes the anatomical features to provide an initial alignment and a digitized representation of the organ surface to further hone the registration.

As part of this procedure, the organ is typically prepared for surgical presentation by mobilizing it from surrounding anatomy which may be followed by stabilization with surgical packing. These techniques inherently impart deformation, altering the intraoperative organ state from preoperative imaging. If an accurate solution to correcting for this deformation could be achieved, there is little doubt that the utility of image guided liver surgery (IGLS) would be enhanced. Deformations have been documented with signed closest point distances varying as +/-

2 cm [REF]. Various methods of deformation correction have been presented in the literature. In recent work, a mechanics-based nonrigid registration method proposed by Rucker et al. has shown a distinct ability to further reduce target error following rigid alignment using sparse data.[23] This approach centers on a biomechanical model mechanically deforming the preoperative organ model (based on the preoperative images) to match a sparse digitization of the intraoperative anterior organ surface. A particular benefit of this method is that it requires no additional information to that routinely acquired for the rigid registration.

An ongoing study at Memorial Sloan Kettering Cancer Center is underway that has demonstrated in a series of clinical data sets promising results for the protocol outlined above. Interestingly, in the process of analyzing that data, it was observed that in each case a different acquisition pattern, or strategy, was used to digitize the intraoperative organ surface by the surgeon, i.e. a different *modus operandi*. A selection of data highlighting this observation is presented in Figure 1. This observation raises the question: how robust are current clinical IGLS methods to variations in clinical surface digitization?

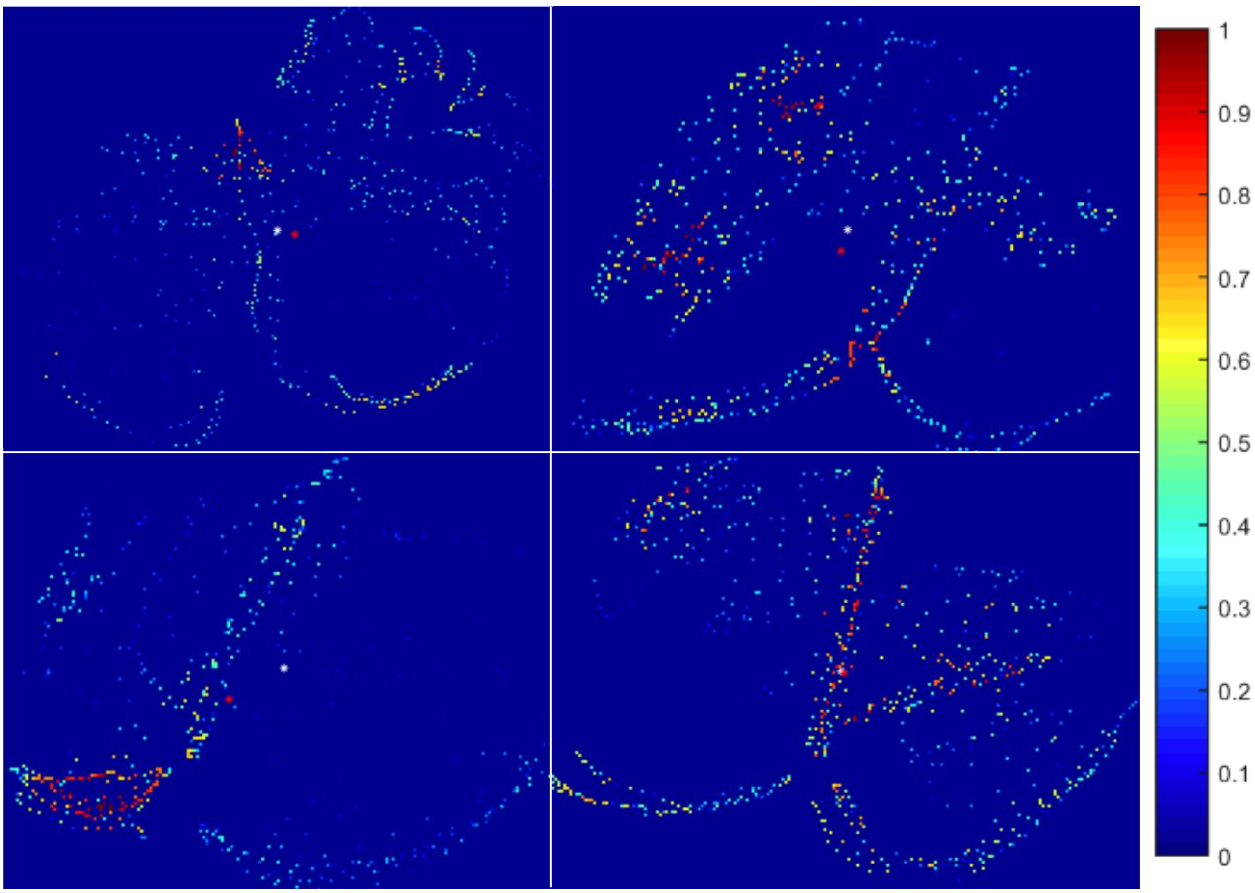

Figure 1: Each panel presents a unique set of clinical surface data represented in 2D. Each panel is oriented such that the inferior ridges run horizontally across the lower section of the image. The color value at each point represents the relative density of neighboring points within a 2 cm radius. A white asterisk in each panel represents the center of the geometric extent of the data in 2D. A red asterisk represents the true centroid of the collected data. It is important to note that each case has a unique distribution of points in relation to the salient-features.

1.2 Previous Work

A number of studies have investigated IGLS registration in open surgical cases. This alignment is often determined by using point-based or surface-based methods. In point-based registration, corresponding points are acquired in both data spaces. These points may consist of anatomical landmarks or artificial fiducial markers. Point-based registration methods then determine an optimal transformation to minimize the error between corresponding points. Point-based methods are highly influenced by fiducial localization error (FLE), or the ability to accurately delineate a point. This method is not readily applicable to the hepatic domain, as the liver surface is poor for localizing a rigid anatomic landmark. Other methods of rigid registration seek to align corresponding surfaces rather than points. Iterative in nature, these algorithms search to minimize some error function, such as residual surface 'fit' error. For example, the iterative closest point (ICP) algorithm conducts a series of point-based registrations, determining a new point correspondence at each iteration by a closest point operator.[24] These types of methods are limited in their ability to determine true correspondence and are therefore dependent upon a reasonable initial orientation. Cash et al. described a method of rigid registration for IGLS that determines an initial organ alignment through a point-based fiducial registration which is then followed by an ICP registration. However this method was still influenced by FLE.[19,25] The current protocol for surface-based rigid registration was introduced by Clements et al.[18] Their salient-feature based weighted ICP method performs an initial alignment by first weighting reliable anatomical surface features and in later iterations equally weights the full organ surface.

A review by Hawkes et al. identified limitations of rigid-based registrations in soft tissue environments.[26] Organ mobilization from the surrounding abdominal supporting ligamenture often introduce nonrigid deformations that alter the intraoperative organ state from its preoperative

image counterpart. A number of groups have investigated model-based deformation correction techniques. Lange et al. published an algorithm using b-splines to deform preoperatively acquired vessels to intraoperative vessels acquired from tracked ultrasound.[22] Miga et al. proposed a mechanical model driven by laser range scan (LRS) surface acquisition which was validated with residual surface error.[27] Cash et al. introduced an incremental finite element model (FEM) approach.[28] Following rigid registration, the model was deformed to fit intraoperative surface data. Dumpuri et al. introduced a surface Laplacian based filter to determine boundary conditions in an extrapolative manner that drove a fit between the preoperative model and intraoperative surface.[29] Most recently, Rucker et al. describes an algorithm which uses a posterior displacement surface to iteratively solve deformations to optimally minimize partial surface fit between surfaces.[23] Both Dumpuri and Rucker methods were validated using phantom subsurface targets as well as residual surface error in clinical cases. The realization of a dataset which incorporates clinical-quality surface characterization in addition to a wealth of subsurface targets, as seen in phantom, would be largely beneficial to the problem of characterizing uncertainty within IGLS.

1.3 Contributions

Rigid and nonrigid registration methods are currently used to align intraoperative physical space with preoperative image space, providing more utility from preoperative imaging in the surgical setting. Both methods of registration rely upon accurate digitization of the intraoperative organ surface. Across the data collection of a series of clinical cases, we observed a high variability in the pattern and density of acquired surfaces. The goal of this work is to characterize the extent to which variation of input data affects the output of clinically relevant image-to-physical registration methods. In order to do so, a data set consisting of multiple realistic surface acquisitions of the same intraoperative organ was required. This data was realized by virtually

projecting the collection pattern of 14 clinically acquired hepatic surfaces onto an anthropomorphic liver phantom that was created with the specification that it reproduce clinically similar deformation patterns seen in the operating room. With this simulated set of data, we were able to observe the effect that varying surface collection has on target error and repeatability following rigid and nonrigid registrations. In addition, a strategy for normalizing, or resampling, collected surface data was developed and applied to the simulated data sets. Results of this work suggest (1) the technique of surface acquisition has downstream effects on registration error and (2) a surface resampling strategy may be used to normalize data acquisition across cases, and users, to further increase the accuracy of current clinical methods.

CHAPTER 2

Methodology

2.1 Data Collection and Registration

Clinical Data Collection

A selection of clinical data representing 14 patients undergoing open liver resection at Memorial Sloan Kettering Cancer Center is presented within this study. Patients were consented and enrolled in an ongoing study approved by the Memorial Sloan Kettering Cancer Center Institutional Review Board. Prior to surgery, contrast enhanced computed tomography (CT) images were acquired from each patient to generate 3D anatomical organ models using surgical planning software (Scout™ Liver, Analogic Corporation, Peabody, MA). Following this processing, the preoperative organ model was loaded into a surgical navigation system (Explorer™ Liver, Analogic Corporation, Peabody, MA). During surgery, after organ mobilization, a series of anatomical features were digitized by manual swabbing with an optically tracked stylus. This digitization creates a sparse 3D point cloud representing the physical surface of anatomical features such as the falciform ligament and inferior ridges. The anterior organ surface was then characterized in the same fashion. A visualization of intraoperative surface collection is presented in Figure 2.

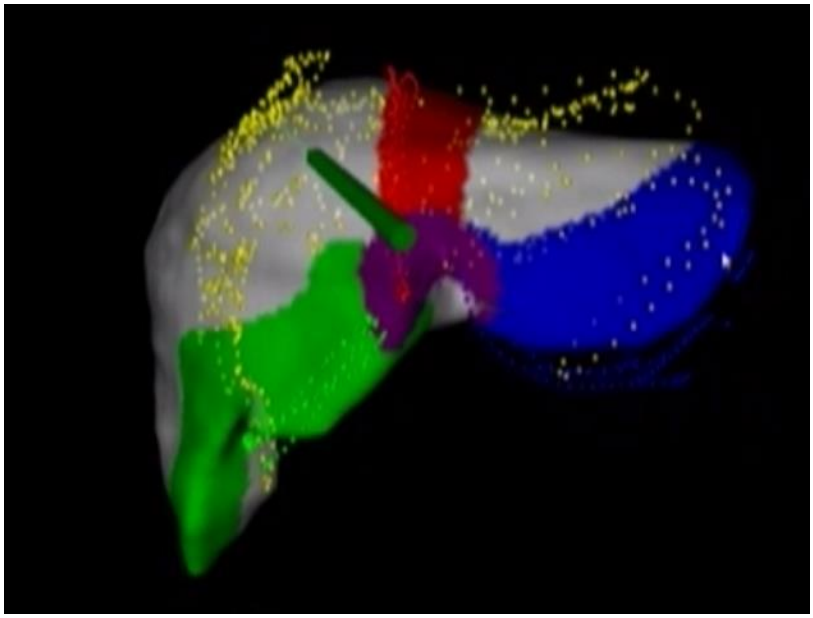

Figure 2: The manual surface digitization interface within the Explorer™ Liver navigation system highlighting a surface alignment generated with the salient-feature wICP method.

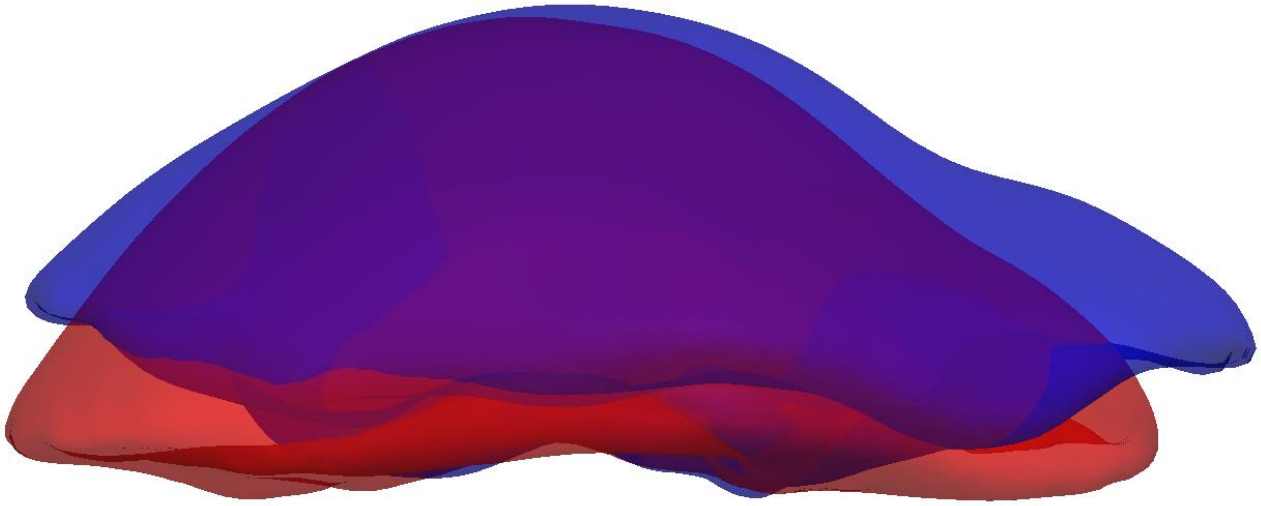

Figure 3: The red surface is the preoperative phantom. The blue surface represents the phantom after it has undergone deformation. Both phantom models were acquired from CT.

Phantom Data Collection

Phantom data utilized in this study was previously reported by Rucker et al.[23] A compliant hepatic phantom was created to mimic clinical observations of organ deformation gathered from a 75 patient multi-center clinical trial.[30] The phantom consisted of a cryogel of water, Polyvinyl alcohol, and glycerin[31] and incorporated 47 subsurface plastic beads which served as ground truth target locations. Similarly to clinical cases, a "preoperative" CT scan of the phantom in undeformed state was acquired to generate an organ model and to identify initial target locations. Next, as seen in Figure 3, the phantom was deformed by altering the posterior organ support surface, simulating the clinical organ mobilization procedure. Salient feature data were collected using optical swabbing in this deformed state. An "intraoperative" CT scan of the deformed phantom was then captured to acquire (1) the true deformed organ volume, (2) the deformed target locations, and (3) a full extent and highly dense digitization of the deformed phantom surface.

Rigid Registration

A robust rigid alignment of image and physical space was determined with a weighted anatomical feature iterative closest point algorithm (ICP).[18] The traditional ICP algorithm iteratively estimates a transformation needed to minimize the closest point distance between source and target surface data. The employed weighted ICP method utilizes homologous anatomical features to bias point correspondence estimation at each iteration. The biased weighting scheme is dynamic through iterations of the algorithm allowing the anatomical features to produce a robust initial alignment while providing support to the digitized organ surface in later iterations. The algorithm provides a transformation which minimizes residual error between preoperative and intraoperative organ surface data.

Biomechanical Model

A linear elastic model of the preoperative organ is precomputed. The patient-specific model assumes that the liver is an isotropic solid. 3D Navier-Cauchy equations are used to describe the tissue mechanics in the following form:

$$\frac{E}{2(1+v)(1-2v)}\nabla(\nabla \cdot u) + \frac{E}{2(1+v)}\nabla^2 u = 0 \quad (1)$$

E is Young's modulus, v is Poisson's ratio, and u is the displacement vector. The system of partial differential equations (PDE) may be solved by applying the Galerkin weighted residual method using linear basis functions. Using this method, the set of PDEs defining nodal displacement vectors, u, are compiled into the following standard linear system of equations in matrix form:

$$[K]\{u\} = \{f\} \quad (2)$$

where K is the $3n\ x\ 3n$ global stiffness matrix, u is the vector of nodal displacements, and f contains the applied body forces and boundary conditions. With respect to the correction methodology, displacement boundary conditions are assumed to be present on organ posterior support surfaces and where the majority of deformation is present. As a result, the model system shown in equation (2) can be pre-computed to ensure fast intraoperative registrations.

Deformation Correction

Nonrigid registration techniques are used to further improve the alignment between image and physical space in an array of applications. In the surgical setting, the organ is first mobilized from abdominal parenchyma and ligamenture. Surgical packing may also be placed beneath the organ to improve presentation. These changes in support manifest as deformations in comparison to the preoperative organ configuration. This study utilizes the nonrigid registration method

introduced by Rucker et al.[23] The method assumes that the significant amount of organ deformation observed intraoperatively is caused by changes to the support surface, i.e. the organ posterior. A parameterized posterior displacement field is iteratively deformed to minimize residual error between the intraoperatively collected surface digitization and the model surface. The result is a prediction of the deformed organ based on the preoperative biomechanical model and sparse intraoperative organ surface data.

The organ support surface is defined as a smoothly varying bivariate 3rd degree polynomial as follows:

$$d_s = \hat{n}_s \sum_{1 \le i+j \le n} c_{ij} t_1^i t_2^j \tag{4}$$

where d_s is the displacement vector for a point on the control surface, $\hat{n}_s$ is the average unit normal vector over the specified support region, and t_1 and t_2 are the tangential coordinates of the point on the support surface. The polynomial constants c_{ij} define the displacement field over the support region. The sum $1 \le i + j \le n$ enforces the polynomial degree and also avoids redundancy in optimization by excluding solely rigid solutions. The principle of superposition allows for rapid determination of model solutions given a linear combination of polynomial coefficients c_{ij}. The displacement field solution for each of the coefficients c_{ij} is precomputed and stored in a matrix, *M*, where each column is the displacement d_{ij} obtained by solving (4) with the right hand side vector computed with c_{ij} = 1 and all other coefficients set to zero, resulting in the following equation for rapid model solving:

$$\{d\} = [M]\{c\} \tag{5}$$

where c is the vector of coefficients. The solved displacement field is then applied to the biomechanical model as a set of Dirchlet boundary conditions.

After computing a model solution for a given c, the rigid alignment may be updated to improve the fit between deformed model and intraoperative surface. A six degree of freedom rigid body transformation is applied to the deformed model using a traditional ICP registration. Thus, the set of parameters used to generate the model displacement is:

$$P = \{c, t_x, t_y, t_z, \theta_x, \theta_y, \theta_z\} \tag{6}$$

The Levenberg-Marquardt algorithm is employed to evaluate the optimal parameter set by minimizing the following function:

$$F = \frac{1}{N}\sum_{i=1}^{N}(\hat{n}_{ci}^{T}(p_{di} - p_{ci})^2) + \alpha E^2 \tag{7}$$

where N is the number of intraoperatively collected surface points, p_{di} are the Cartesian coordinates of the i^{th} collected surface point, p_{ci} are the Cartesian coordinates of the corresponding i^{th} point on the deformed model surface (point correspondence is estimated using closest Euclidean distance), and $\hat{n}_{ci}^{T}$ is a unit vector normal to the model surface at p_{ci}. E is an energy constraint representing total strain energy in the displacement field and is solved by $E = d^t K d$. The term αE^2 serves to regularize distortion across the deformation field. The method is initialized via rigid registration using the salient feature weighted ICP method. Optimization is executed a set number of iterations or until a convergence threshold is met.

Creation of Simulated Data

To observe the effect that intraoperative organ surface digitization techniques have on registration results we required a set of data that consisted of multiple distinct acquisitions of the same deformed organ surface. Additionally, known target locations are required to quantify registration results. To achieve this data, the surface data patterns of 14 clinical data collections were used to generate new surface acquisitions of a well-characterized hepatic phantom. As an overview, the clinical surface data was rigidly aligned to the phantom, scaled to account for differences in organ size, and projected onto the intraoperative phantom surface. To begin, the clinical surface and feature data were rigidly registered to the analogous phantom data using the previously described salient-feature weighted ICP algorithm. This method ensured that the source and target data were physically aligned in accordance to the salient features but did not account for differences in (1) organ size or (2) the extent of collected surface data. An affine registration method was then employed to scale the clinical surface data to the same bounds as the true deformed anterior phantom surface. The applied affine method was the finite ICP method by Kroon which allowed for the inclusion of scale, s, and shear, τ, in the optimization of the transformation matrix.[32] The method works by optimizing the following parameter set to best minimize the error between source and target points.

$$P = \{t_x, t_y, t_z, \theta_x, \theta_y, \theta_z, s_x, s_y, s_z, \tau_{xy}, \tau_{xz}, \tau_{yx}, \tau_{yz}, \tau_{zx}, \tau_{zy}\} \quad (8)$$

Following the transformation of intraoperative clinical organ surface swabs to our mock "intraoperative" phantom surface, the clinical data points could be projected to their closest point on the mock "intraoperative" phantom CT, producing a set of 14 independent, clinically-relevant patterns of realistic "intraoperative" data acquisition on the phantom surface.

2.2 Proposed Data Resampling Method

The goal of our proposed approach is to better approximate the underlying intraoperative organ surface from the collected sparse surface digitization. The basic structure of the method is depicted by the flowchart in Figure 4. In overview, a surface is fit to the sparsely collected data. That surface is then discretized to produce a consistent surface characterization for registration input.

An assumption was made that the anterior organ surface, from which the sparse surface data was collected, may be treated as a bounded, continuous, and unique surface of the form:

$$z = f(x, y) \tag{9}$$

To robustly treat this data with this form, a rigid-body transformation is determined which optimally projects the surface data onto the $x - y$ plane. A 3D least squares plane is fit to the sparse surface data. The normal to that plane, which intersects the centroid of the data, is considered the mean surface normal. By transforming the mean surface normal to the $z -$ axis, the 3D least squares plane that best fits the surface data is aligned with the $x - y$ plane. The required axis of rotation is the vector orthogonal to the surface normal and $z -$ axis. An angle of rotation, is calculated between the two vectors about this axis. Rodrigues' rotation formula is then used to determine the rotation which transforms the input surface to the optimal projection on the $x - y$ plane:

$$v_{rot} = vcos\theta + (K \times v)sin\theta + K(K \cdot v)(1 - cos\theta) \tag{10}$$

where v is a vector in $\mathbb{R}^3$, K is a unit vector describing an axis of rotation, and θ is an angle of rotation.

A surface is then fit to the transformed data using the surface modeling tool gridfit.[33] Gridfit approximates a surface by fitting a rectangular grid to sparse data and then approximating values across the grid. Interpolation at a point within the grid is a linear combination of values in the local region. Thus the interpolation problem is generalized as a system of linear equations:

$$[A]\{x\} = \{y\} \tag{11}$$

where *x* is a vector representing each grid node and *A* is a matrix with a number of rows equal to the number of input points and a number of columns equal to the number of grid points. At this stage, the system is highly underdetermined. The solution is to attempt to force the first partial derivative of the surface in cells neighboring each grid node to be equal. This results in a second linear system of equations in the form:

$$[B]\{x\} = 0 \tag{12}$$

where the derivatives are estimated using finite differences at neighboring nodes. The system is then solved for *x* such that the following equation is minimized.

$$|[A]\{x\} - \{y\}|^2 + \lambda|[B]\{x\}|^2 \tag{13}$$

In essence, A represents the pull of input data on the grid and B depicts the resistance of the grid. The weighting parameter λ may be altered to control the relative "smoothness" of the resulting surface.

The resulting surface exists as a discretized rectangle on the $x - y$ plane with surface height values of z at each node and 1 mm spacing between nodes. At this point a weighting scheme is applied to the new surface. The surface fitting method approximates data equally in regions of high and low certainty. A weighting strategy was explored to sample more densely in areas of the surface which correspond to collected data. Table 1 depicts all weighting schemes which were

investigated. First, the fitted surface was thinned to achieve a desired minimum spacing between points. Minimum spacing values, presented in the "sparse" column of Table 1, ranging from 1 to 5 mm were evaluated. Next, the true surface data was projected to corresponding closest points on the fitted surface. A square kernel of a specified side length s, and presented as the "dense" column of Table 1, consisting of s^2 points with 1 mm spacing was centered at each projected point. This scheme created dense regions near collected data while ensuring data coverage across the full surface extent. Varying density patterns were investigated to determine viability, including equal sampling across the entire surface.

Next, the fitted surface is trimmed such that it represents a single region which is more accurately bounded by the outer contour of the input data. To accomplish this, the $x - y$ surface is treated as a binary image. The "pixels" that correspond to the collected surface data are given a value of 1. A mask is then created by dilating those "pixels" until they enclose a single, contiguous region which is then filled. Applying the mask to the fit surface creates a set of data more accurately bounded by the input data. The inverse transformation is then applied, returning the newly sampled surface to the original physical space.

Table 1: Summation of resampling weighting scheme results.

		Mean Target Error (mm)		STDEV
Dense	**Sparse**	**"Collected" Nonrigid**	**Resampled Nonrigid**	**Resampled Nonrigid**
1	1	5.15	5.89	0.45
1	2		5.72	0.5
1	3		5.57	0.48
1	5		5.45	0.27
3	2		5.61	0.56
3	3		5.45	0.41
3	5		5.39	0.44
5	2		5.62	0.66
5	3		5.69	0.90
5	5		5.54	0.62
7	2		5.70	0.86
7	3		5.69	0.58
7	5		5.55	0.66

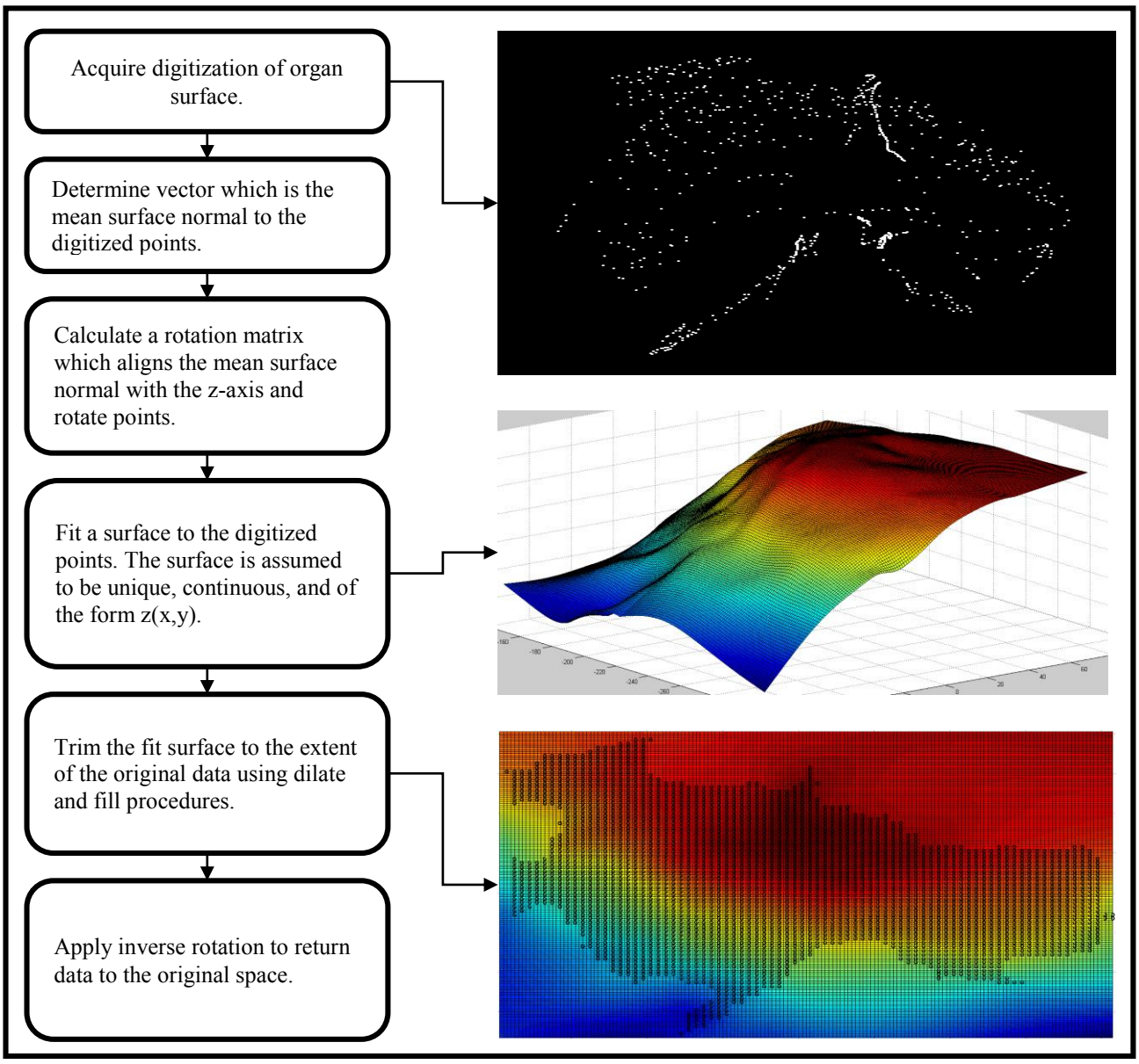

Figure 4: Overview of data resampling methods.

2.3 Validation

Target Registration Error and Reproducibility

The subsurface beads embedded within the phantom provide a representation of true targets for our registration methods. The true initial and final target locations were extracted from the mock "preoperative" and "intraoperative" CTs respectively. The displacement fields provided by rigid registration and nonrigid deformation correction were applied to the preoperative targets in order to predict the final target locations. The Euclidean closest point distance was then calculated between the predicted and true target locations to determine target registration error (TRE), which serves as a true measurement of accuracy.

Due to the wealth of repeated target predictions within the simulated phantom data set, a measurement of precision may be determined. Each of the simulated surface collections produces its own predicted target locations. The variation of predictions at a certain target may be evaluated in order to ascertain method reproducibility. We use mean absolute deviation to quantify precision in this experiment. First, the average prediction at each target is calculated. Mean absolute deviation is the average distance from each prediction to the average prediction. This measurement provides a quantification of each registration method's precision at each target location.

Statistical Testing

Due to the large number of target positions resulting from the simulated data (47 targets each in 14 cases across 4 registration scenarios – rigid collected, nonrigid collected, rigid sampled, nonrigid sampled), a Z-test was used to determine differences in registrations. A Z-test is a statistical test used when the distribution for the test statistic can be approximated by a normal distribution and the sample size is large. A two-tailed test was used with $\alpha = 0.05$.

CHAPTER 3

Results

3.1 Phantom Suitability

Figure 5 depicts four cases of simulated phantom surface data. Each panel represents an independent collection of the deformed phantom surface displayed with the "preoperative" phantom model in red. Each case contains the same set of digitized anatomical features, highlighted in blue. Regional point density within the surface data is observed to vary across cases in a similar manner to what was observed in the original clinical data.

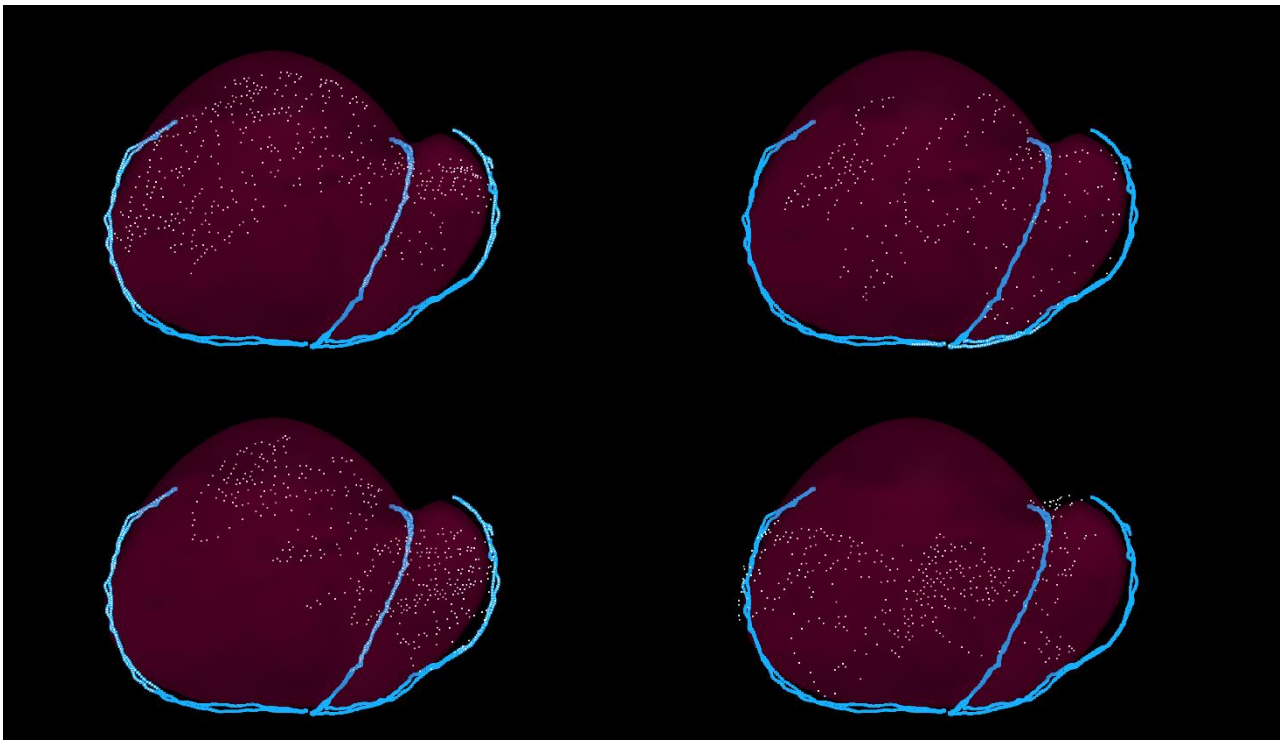

Figure 5: Each panel presents a unique set of collected surface data rigidly registered to the "preoperative" organ model in red. Independent surface digitization of the deformed organ state are shown in white and identical demarcations of the deformed salient features are in blue. It is important to note that each case has a unique distribution of points in relation to the salient features.

Figure 6 displays a qualitative analysis of the suitability of the simulated phantom data. The figure presents rigid registration results for (a) a clinical case and (b) the phantom case utilized in this study. The registered model surface is colored by the signed closest point distance to the surface data. Qualitatively, the phantom model depicts a similar deformation to what is observed clinically. In general, a flattening of the organ is observed which occurs by raising the outer segments of the organ while the center is lowered.

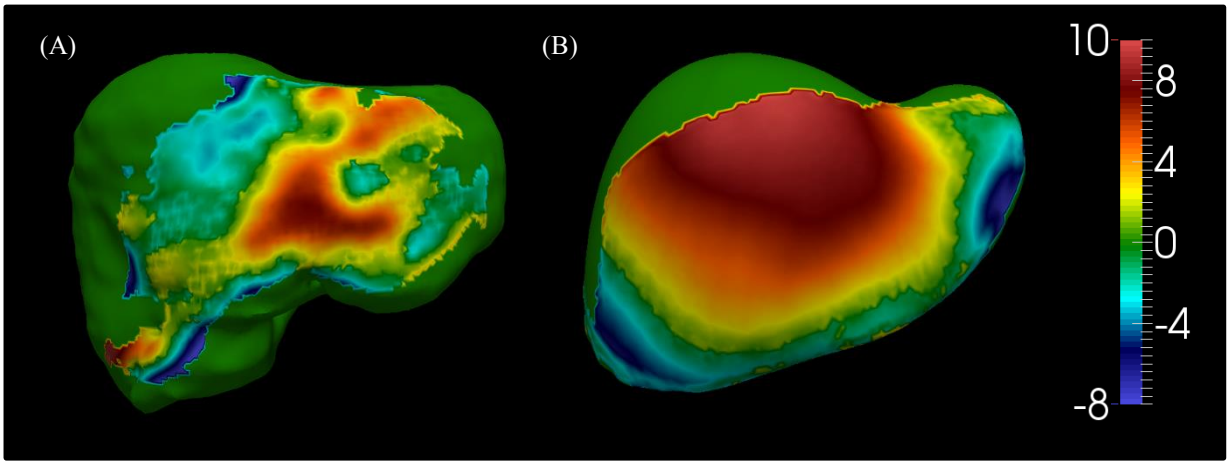

Figure 6: Results from (A) a clinical case following rigid registration and (B) the phantom case following rigid registration. The registered model surface is colored by the signed closest point distance to the intraoperative surface data. The phantom presents a similar deformation pattern to the clinical case.

3.2 Surface Resampling

Figure 7 represents four cases of resampled phantom surface data. The resampled cloud enforces a minimum point spacing of 1 mm, in dense regions, and a maximum spacing of 3 mm, in sparse regions. The higher point density was achieved in areas representing the original collected surface. The resampled data and original data are similar in overall extent. Qualitatively, the resampled surface achieves a suitable approximation of the collected surface. This qualitative result is supported by a residual error of 0.91 mm between the collected and resampled surfaces.

The current resampling method produces an accurate approximation of the underlying organ surface as it is identified by intraoperative digitization.

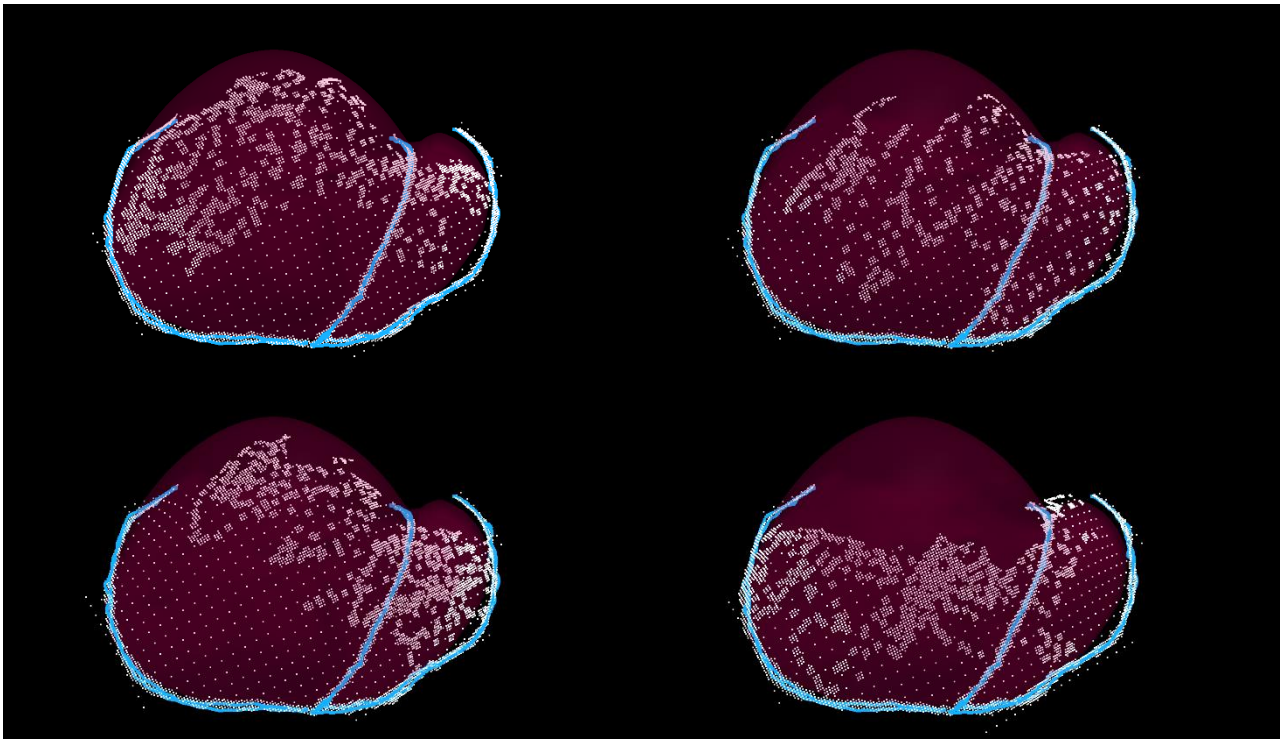

Figure 7: Each panel presents a unique set of resampled surface data rigidly registered to the "preoperative" organ model in red. Resampled surface digitizations of the deformed organ state are shown in white and identical demarcations of the deformed salient features are in blue. It is important to note that while each case has a unique distribution of points in relation to the salient features, they all share a more uniform extent of coverage.

The weighting schemes investigated in this experiment are presented in Table 1. The full set of data, 14 cases with 47 targets each, was evaluated with each weighting strategy. The TRE mean and standard deviation for each scheme are presented in comparison to the nonrigid TRE results from using collected data. The sparse value represents an underlying minimum point distance that is enforced across the full extent of the surface. The dense value for each scenario represents the side dimensions of the square kernel centered at each true data point projected on the resampled surface where 1 mm spacing is enforced. The scheme of 3 (dense) and 5 (sparse)

presented the lowest mean TRE and is therefore presented as the sampled result throughout this paper.

3.3 Quantitative Registration Results

Rigid and nonrigid registration methods were employed on 14 cases of both collected and resampled data sets. With 47 targets per case, a total of 658 target locations were predicted using each of the four registration scenarios: (1) rigid registration with raw collected data, (2) nonrigid registration with raw data, (3) rigid registration driven with resampled surface data, and (4) nonrigid registration driven with resampled data. Figure 8 displays 7 true target locations in white with the associated 14 predictions from nonrigid registration using collected data in pink and nonrigid registration using resampled data in blue.

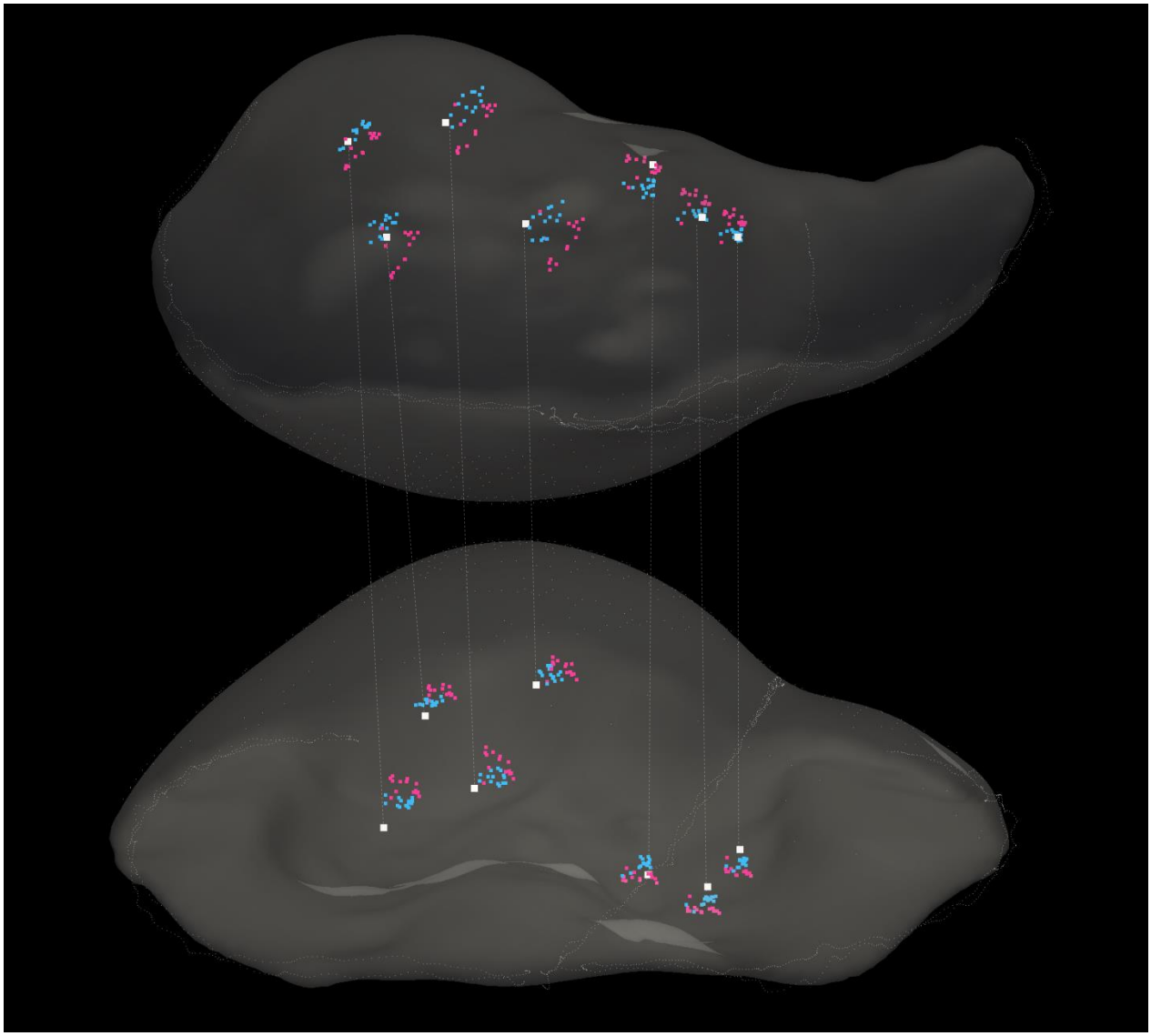

Figure 8: Locations of 7 fiducial targets are shown in the deformed phantom volume from two perspectives. The white square indicates the true target location. The pink and blue squares represent the 14 predictions of each target generated using the collected and resampled data, respectively, as the input surface data for the nonrigid registration method. The resampled predictions provide a more reproducible result, indicated by their tighter clustering ($p < .001$). The resampled data also provides a more accurate prediction for the displayed points, however this trend is not significant across the full set of targets ($p > .05$).

Registration Accuracy

TRE is a measurement of prediction accuracy and represents the distance from each predicted target to the true target. Figure 9 presents a box plot of the average TRE for each case of surface data evaluated with each registration scenario. Nonrigid registration, with both collected and resampled data, produced a more accurate average target prediction. Additionally, resampling surface data provided a more accurate rigid registration. Figure 10 presents a statistical histogram of the full distribution of TRE for each case of surface data evaluated with each registration scenario. A Z-test was used to test for statistical significance between the TRE distributions resulting from each of the registration scenarios. Nonrigid registration using collected data ($p < .001$), nonrigid registration using resampled data ($p < .001$), and rigid registration using resampled data ($p < .05$) were each found to have significantly lower TRE than rigid registration using collected data. Additionally, both nonrigid registration methods ($p < .001$) were found to produce TRE significantly lower than rigid registration using resampled data. However, no statistical difference was determined to lie between the collected nonrigid registration, average TRE of 5.15 mm, and resampled nonrigid registration, average TRE of 5.39 mm ($p > .05$). Nonrigid registration using collected data resulted in TRE ranging from 0.9 mm to 17.1 mm while nonrigid registration using resampled data resulted in TRE ranging from 0.7 mm to 14.8 mm.

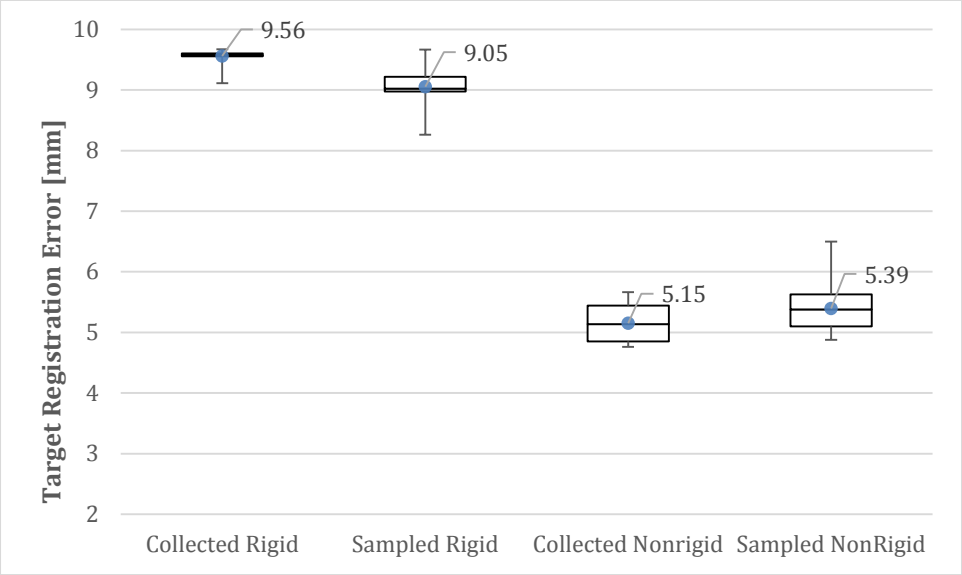

Figure 9: Box plot representing the distribution of average TRE for each case of surface data (14 data points) and each method of registration. TRE is a measurement of prediction accuracy and represents the distance from each predicted target to the true target. Statistical significance exists between each interaction ($p < .05$) except when comparing the Collected and Sampled NonRigid results ($p > .05$).

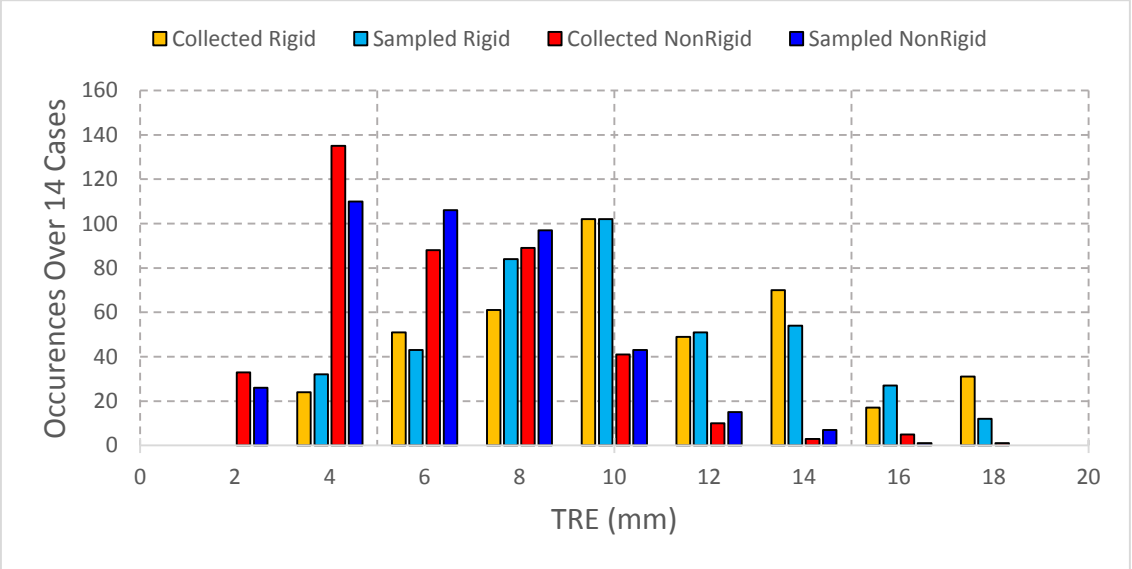

Figure 10: Statistical histogram of the 658 target errors resulting from four different registration scenarios. Yellow and Cyan – The results of a rigid registration using the weighted patch ICP method of [18], using "collected" data and resampled data respectively. Red and Blue – The results of a nonrigid registration using the method of [23] using "collected" and resampled data respectively. Statistical significance exists between each interaction ($p < .05$) except when comparing the Collected and Sampled NonRigid results ($p > .05$).

Registration Reproducibility

Reproducibility is a measurement of the ability of a particular study to be replicated and is determined by calculating the distance from each predicted target to the average prediction of that particular target across all cases. In this study, reproducibility amounts to the ability of the registration method to replicate target predictions given different input data. Figure 11 presents a box plot of the average reproducibility for each case of surface data evaluated with each registration scenario. Rigid registration with both collected and resampled data presents more reproducible target predictions than either nonrigid method. Nonrigid registration using resampled data provides a more reproducible target prediction than nonrigid registration with collected data. Figure 12 presents a histogram of the full distribution of target prediction reproducibility for each case of surface data evaluated with each registration scenario. A Z-test was used to test for statistical significance between the resulting distributions. Nonrigid registration using resampled data was found to be statistically more reproducible than nonrigid registration using collected data ($p < .001$). Additionally, all other reproducibility distributions resulting from the different registration methods were determined to be significantly different from one another ($p < .001$).

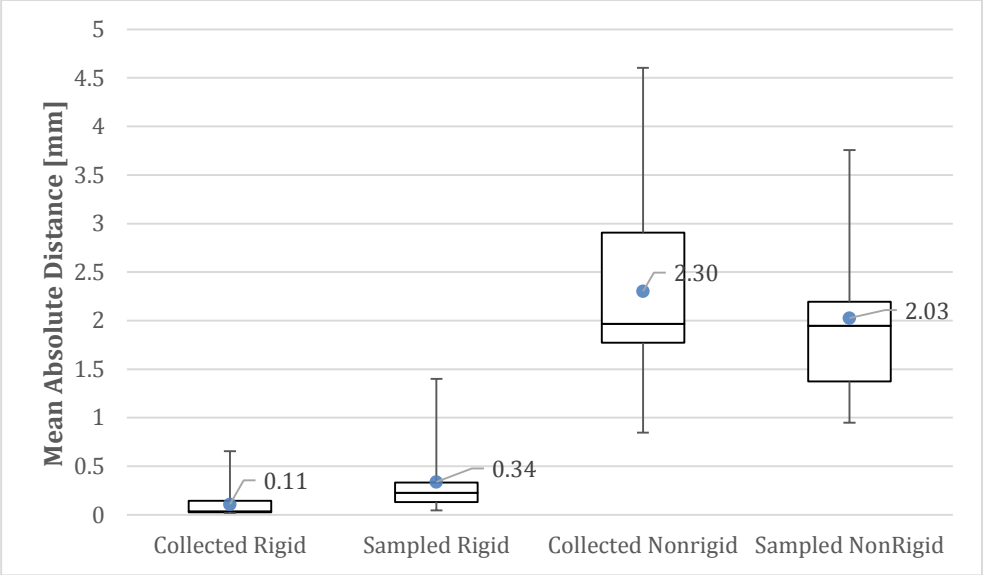

Figure 11: Box plot representing the distribution of average reproducibility for each case of surface data (14 data points) and each method of registration. Reproducibility is a measurement of precision and represents the distance from each predicted target (658) to the set of average targets (47). Statistical significance exists between each interaction ($p < .001$.

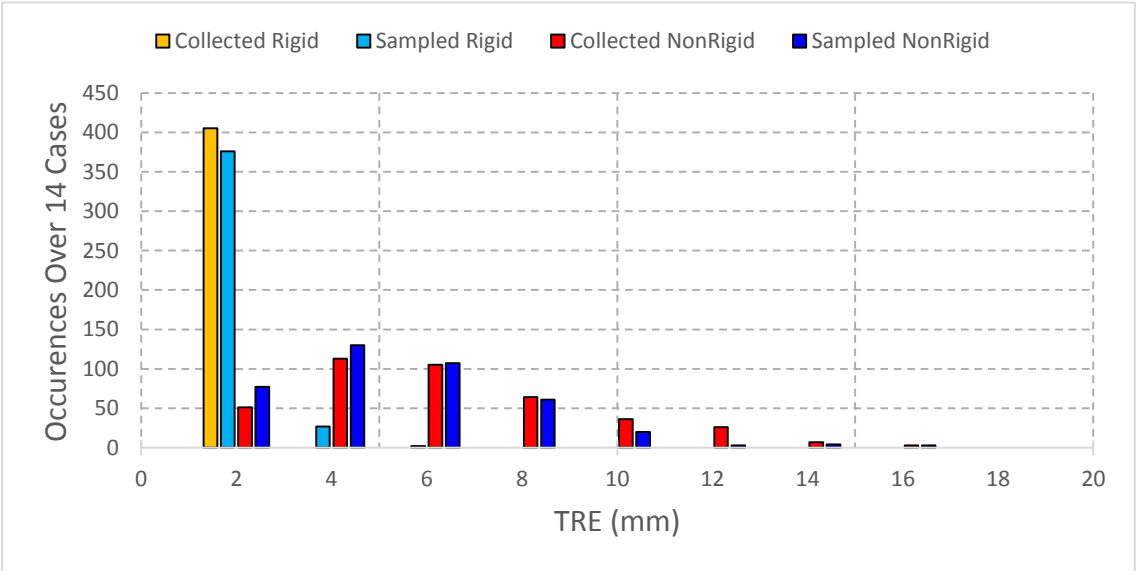

Figure 12: Statistical histogram of the 658 target precisions resulting from four different registration scenarios. Yellow and Cyan – The results of a rigid registration using the weighted patch ICP method of [18], using "collected" data and resampled data respectively. Red and Blue – The results of a nonrigid registration using the method of [23] using "collected" and resampled data respectively. Statistical significance exists between each interaction ($p < .001$).

CHAPTER 4

Discussion

The distribution of TRE illustrated by the histogram in Figure 9 shows an average improvement in TRE from 9.6 mm to 5.2 mm over the 14 phantom cases when employing the nonrigid registration approach of Rucker et al.[23] However, while the average TRE was 5.2 mm, individual TRE values ranged from 0.9 mm to 17 mm. Nonrigid registration using resampled data presented a statistically similar average TRE of 5.4 mm with a tighter range of individual errors (0.7 mm to 14.8 mm). The difference in methods is better described by their reproducibility, or precision, in making target predictions. Nonrigid registration using the preprocessed resampled data produced a statistically tighter clustering of target predictions than nonrigid registration using the original collected data. The 14 case study suggests that the resampling of sparse surface data results in a nonrigid registration that is more robust to variations in input data. While future work is still required to better understand the technique of surface data resampling, to our knowledge the results of this study are the first to investigate surgical modus operandi with respect to impact on rigid and nonrigid image-to-physical registration methods for soft-tissue image guided surgery. The results suggest considerable variability and that resampling strategies may be a good way to provide more reproducible nonrigid registrations.

CHAPTER 5

Conclusions

The goal of this study was to characterize the effect that variations in digitization of the intraoperative organ surface have on downstream image-to-physical registration methods in IGLS. To observe this effect, a set of data was manufactured which consisted of multiple clinically relevant acquisitions of the same deformed organ surface. We conclude from our study that uncertainty is introduced into nonrigid registration results by variations in the initial surface digitization, creating a clinical method with suboptimal reproducibility. A method for preprocessing clinical surface data was introduced which significantly improved the reproducibility, or precision, of our nonrigid registration method without negatively impacting accuracy. Additionally, the surface data resampling method is realized for a sparse data environment which creates the potential for its adaptation into any surface-based soft tissue guidance setting. Future work will entail further study and refinement of the method of data resampling.

REFERENCES

[1] American Cancer Society. (2015). Cancer Facts and Figures. Retrieved June 19, 2015 from (http://www.cancer.org/acs/groups/content/@editorial/documents/document/acspc-044552.pdf).

[2] Borner MM. (1999). Neoadjuvant chemotherapy for unresectable liver metastases of colorectal cancer: too good to be true? *Ann Oncol **10**:623-626.*

[3] Steele G Jr and Ravikumar TS. (1989). Resection of hepatic metastases from colorectal cancer: Biologic perspective. *Ann Surg **210**:127-138.*

[4] Wood CB, Gillis CR, Blumgart LH. (1976). A retrospective study of the natural history of patients with liver metastases from colorectal cancer. *Clin Oncol **2**:285-288.*

[5] Wagner JS, Adson MA, Van Heerden JA, et al. (1984). The natural history of hepatic metastases from colorectal cancer: A comparison with respective treatment. *Ann Surg **199**:502-508.*

[6] Tomlinson JS, Jarnagin WR, DeMatteo RP, et al. (2007). Actual 10-year survival after resection of colorectal liver metastases defines cure. *J Clin Oncol **25(29)**:4575-4580.*

[7] Fong Y, Fortner J, Sun RL, et al. (1999). Clinical score for predicting recurrence after hepatic resection for metastatic colorectal cancer: Analysis of 1001 consecutive cases. *Ann Surg **230**:309-318.*

[8] Scheele J, Stang R, Altendorf-Hofmann A, et al. (1995). Resection of colorectal liver metastases. *World J Surg **19:59**-71.*

[9] Jamison RL, Donohue JH, Nagorney DM, et al. (1997). Hepatic resection for metastatic colorectal cancer results in cure for some patients. *Arch Surg **132**:505-510.*

[10] Choti MA, Sitzmann JV, Tiburi MF, et al. (2002). Trends in long-term survival following liver resection for hepatic colorectal metastases. *Ann Surg **235**:759-766.*

[11] Kopetz S, Chang GJ, Overman MJ, et al. (2009). Improved survival in metastatic colorectal cancer is associated with adoption of hepatic resection and improved chemotherapy. *J Clin Oncol **27(22)**: 3677-3683.*

[12] U.S. Cancer Statistics Work Group. (2014). United States cancer statistics: 1999-2011 incidence and mortality web-based report. Atlanta(GA): Department of Health and Human Services, Centers for Disease Control and Prevention, and National Cancer Institute.

[13] Manizate F, Hiotis SP, Labow D, et al. (2010). Liver functional reserve estimation: state of the art and relevance to local treatments. *Onc **78(1)**:131-134.*

[14] Abdalla EK, Adam R, Bilchik AJ, et al. (2006). Improving resectability of hepatic colorectal metastases: expert consensus statement. *Ann Surg Onc **13(10)**:1271-1280.*

[15] Correa-Gallego C, Fong Y, Gonen M, et al. (2014). A retrospective comparison of microwave ablation vs. radiofrequency ablation for colorectal cancer hepatic metastases. *Ann Surg Onc* ***21(13)****:4278-4283.*

[16] Leung U, Kuk D, D'Angelica MI, et al. (2014). Long-term outcomes following microwave ablation for liver malignancies. *Brit J Surg* ***102(1)****:85-91.*

[17] Alexander ES, Wolf FJ, Machan JT, et al. (2015). Microwave ablation of focal hepatic malignancies regardless of size: a 9-year retrospective study of 64 patients. *Eur J Rad* ***84(6)****:1083-1090.*

[18] Clements LW, Chapman WC, Dawant BM, et al. (2008). Robust surface registration using salient anatomical features for image-guided liver surgery: algorithm and validation. *Med Phys* ***35(6)****:2528-2540.*

[19] Cash DM, Sinha TK, Chapman WC, et al. (2003). Incorporation of a laser range scanner into image-guided liver surgery: surface acquisition, registration, and tracking. *Med Phys* ***30****:1671.*

[20] Lathrop RA, Hackworth DM, and Webster RJ. (2010). Minimally invasive holographic surface scanning for soft-tissue image registration. *IEEE Trans BME* ***57(6)****:1497-1506.*

[21] Peterhans M, von Berg A, Dagon B, et al. (2011). A navigation system for open liver surgery: design, workflow and first clinical applications. *Int J Med Rob and Comp Assist Surg* ***7(1)****:7-16.*

[22] Lange T, Eulenstein S, Hunerbein M, et al. (2003). Vessel-based non-rigid registration of MR/CT and 3D ultrasound for navigation in liver surgery. *Comp Aid Surg* ***8(5)****:228-240.*

[23] Rucker DC, Wu Y, Clements LW, et al. (2014). A mechanics-based nonrigid registration method for liver surgery using sparse intraoperative data. *IEEE Trans Med Im* ***33(1)****:147-158.*

[24] Besl PJ and McKay ND. Method for registration of 3-d shapes. *IEEE Trans Pattern Anal Mach Intell* ***14****:239-256.*

[25] Cash DM, Miga MI, Glasgow SC, et al. (2007). Concepts and preliminary data toward the realization of image-guided liver surgery. *J Gastrointest Surg* ***11(7)****:844-859.*

[26] Hawkes D, Barratt D, Blackall JM, et al. (2005). Tissue deformation and shape models in image-guided interventions: a discussion paper. *Med Image Anal* ***9****: 163-175.*

[27] Miga MI, Sinha TK, Cash DM, et al. (2003). Cortical surface registration for image-guided neurosurgery using laser range scanning. *IEEE Trans Med Im* ***22****:973-985.*

[28] Cash DM, Miga MI, Sinha TK, et al. (2005). Compensating for intraoperative soft-tissue deformations using incomplete surface data and finite elements. *IEEE Trans Med Im* ***24(11)****:1479-1491.*

[29] Miga MI, Dumpuri P, Simpson AL, et al. (2011). The sparse data extrapolation problem: strategies for soft-tissue correction for image-guided liver surgery. *SPIE Med Im **7964**.*

[30] Dumpuri P, Clements LW, Dawant BM, et al. (2010). Model-updated image-guided liver surgery: preliminary results using surface characterization. *Prog Biophys Mole Biol, **103(1-2)**:197-207.*

[31] Surry KJ, Austin HJ, Fenster A, et al. (2004). Poly(vinyl alcohol) cryogel phantoms for use in ultrasound and MR imaging. *Phys Med Biol **49**:5529-5546.*

[32] Kroon, DJ. (2009). Finite iterative closest point. Matlab Central File Exchange. Retrieved October 15, 2015 from (http://www.mathworks.com/matlabcentral/fileexchange/24301-finite-iterative-closest-point).

[33] D'Errico J. (2005). Surface fitting using gridfit. Matlab Central File Exchange. Retrieved October 8, 2015 from (http://www.mathworks.com/matlabcentral/fileexchange/8998-surface-fitting-using-gridfit).

[34] Wiles AD, Thompson DG and Frantz DD. (2004). Accuracy assessment and interpretation for optical tracking systems. *SPIE Med Im **5367**.*

[35] Clements LW, Dumpuri P, Chapman WC, et al. (2011). Organ surface deformation measurement and analysis in open hepatic surgery: method and preliminary results for 12 clinical cases. *IEEE Trans Bio Eng **58(8)**.*